Article

Effect of Raster Angle and Infill Pattern on the In-Plane and Edgewise Flexural Properties of Fused Filament Fabricated Acrylonitrile–Butadiene–Styrene

Hamza Qayyum [1], Ghulam Hussain [2,*], Muhammad Sulaiman [1], Malik Hassan [3], Aaqib Ali [4], Riaz Muhammad [2], Hongyu Wei [5], Tauheed Shehbaz [6], Muhammad Aamir [7,*] and Khurram Altaf [8]

[1] Faculty of Mechanical Engineering, Ghulam Ishaq Khan Institute of Engineering Sciences and Technology, Topi 23640, Pakistan
[2] Mechanical Engineering Department, College of Engineering, University of Bahrain, Isa Town 32038, Bahrain
[3] School of Engineering, University of Guelph, Thornbrough Building, 50 Stone Road East, Guelph, ON N1G 2W1, Canada
[4] Department of Mechanical Engineering, Michigan State University, East Lansing, MI 48824, USA
[5] College of Mechanical & Electrical Engineering, Nanjing University of Aeronautics & Astronautics, Nanjing 210016, China
[6] Faculty of Material and Chemical Engineering, Ghulam Ishaq Khan Institute of Engineering Sciences and Technology, Topi 23640, Pakistan
[7] School of Engineering, Edith Cowan University, Joondalup 6027, Australia
[8] Department of Mechanical Engineering, Universiti Teknologi PETRONAS, Seri Iskandar 32610, Perak Darul Ridzuan, Malaysia
* Correspondence: ghussain@uob.edu.bh (G.H.); m.aamir@ecu.edu.au (M.A.)

Abstract: Fused Filament Fabrication (FFF) is a popular additive manufacturing process to produce printed polymer components, whereby their strength is highly dependent on the process parameters. The raster angle and infill pattern are two key process parameters and their effects on flexural properties need further research. Therefore, the present study aimed to print test specimens with varying raster angles and infill patterns to learn their influence on the in-plane and edgewise flexural properties of acrylonitrile–butadiene–styrene (ABS) material. The results revealed that the highest in-plane and edgewise flexural moduli were obtained when printing was performed at 0° raster angle. In comparison, the lowest values were obtained when the printing was executed with a 90° raster angle. Regarding the infill pattern, the tri-hexagon pattern showed the largest in-plane modulus, and the quarter-cubic pattern exhibited the greatest edgewise flexural modulus. However, considering both the modulus and load carrying capacity, the quarter-cubic pattern showed satisfactory performance in both planes. Furthermore, scanning electron microscopy was used to investigate the failure modes, i.e., raster rupture, delamination of successive layers and void formation. The failure occurred either due to one or a combination of these modes.

Keywords: fused filament fabrication; raster angle; infill pattern; flexural properties

1. Introduction

Additive manufacturing (AM), often known as 3D printing, has experienced tremendous growth in nearly every engineering sector, especially in the aerospace and automobile industries [1–4]. According to ISO/ASTM 52900 [5], AM technologies are classified into seven classes. Fused filament fabrication (FFF), a sub-class of the material extrusion processes, is one of the most widely used AM technologies owing to its low energy usage, ease of manufacturing complex geometries with fewer tool changes and production times, and lessened waste [6,7]. FFF is based on the production of components by extruding material from a heated nozzle.

The printing process parameters greatly affect the mechanical strength of the printed component. Therefore, a significant amount of work has been done to study the effect

of printing temperature, printing speed, layer height, bed temperature, and infill density on the mechanical properties of printed components using FFF [8–11]. Apart from the aforementioned parameters, raster angle and infill pattern can also affect the mechanical properties of printed components. Raster angle is the angle between the beads being printed with the primary axis of the printer bed, which is mostly an x-axis, as depicted in Figure 1a [12]. While the path along which material is extruded inside the perimeter is called an infill pattern, as illustrated in Figure 1b.
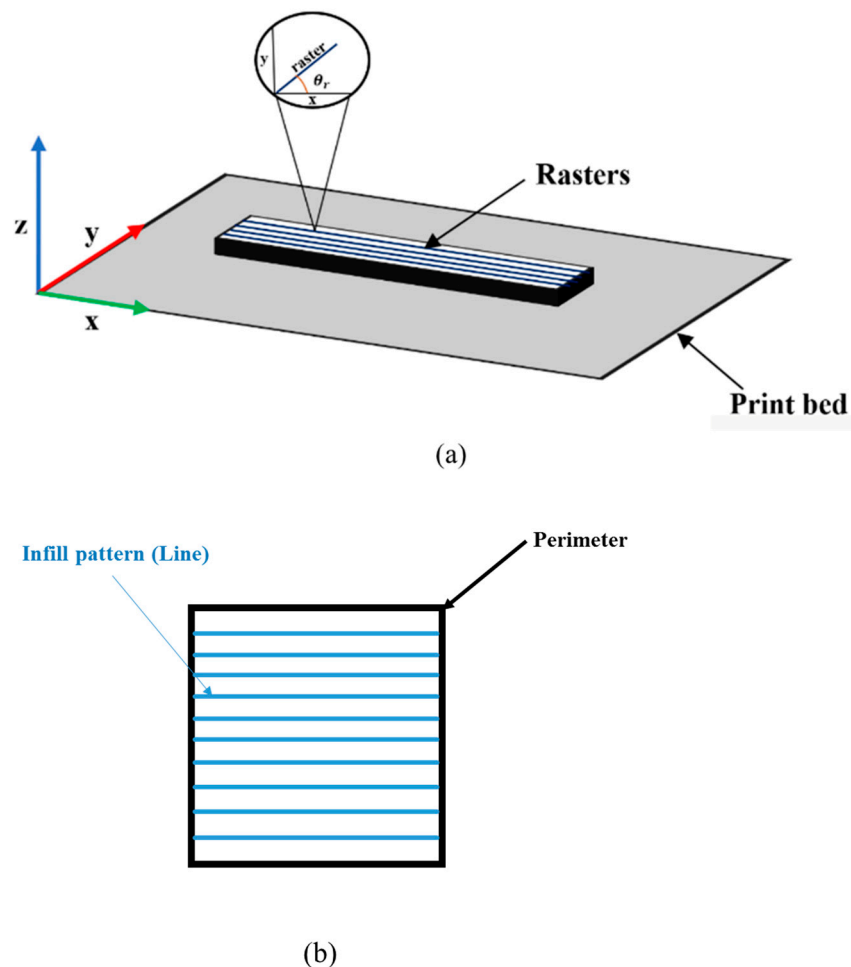

(a)

(b)

Figure 1. Schematic representations (**a**) raster angle (**b**) infill pattern (Line) and perimeter.

Flexural properties are of great importance for composite and sandwich structures. The flexural strength of a structure is its ability to resist bending deflection whenever the load is applied to it [13]. Therefore, these properties are of great interest in the fields where the primary loading condition is flexural such as aerospace and structural applications. The literature has shown various studies regarding the impact of two highly influential process parameters, i.e., raster angle and infill pattern, on the flexural properties. For instance, Byberg et al. [14] experimentally examined flexural properties for 3D printed ULTEM at raster angles of $0°$, $45/-45°$, and $90°$. It was concluded the samples printed at $0°$ raster had the highest flexural modulus among the tested samples. Kaplun et al. [15] suggested that among the samples printed at a $0°$, $45°$, and $90°$, the $0°$ raster angle samples exhibited the highest tensile and fatigue strength. Motaparti et al. [16] and Taylor et al. [17] investigated the flexural properties of ULTEM 9085 and ULTEM 1010, respectively. The coupons were fabricated at two raster angles of $0/90°$ and $45/-45°$. The results revealed that $0/90°$ raster angle with vertical orientation produced samples with a higher flexural strength of about 105 MPa compared to 95 MPa for $45/-45°$ raster [16]. Wu et al. [18] investigated the bending strengths at three different raster angles, i.e., $0/90°$, $30/-60°$, and $45/-45°$.

It was concluded that samples with 0/90° raster showed the highest tensile and bending strengths. In addition, flexural and tensile properties for five different singular raster angles in different printing orientations were evaluated by Durgun and Ertan [19]. It was observed that the samples fabricated in the edgewise direction resulted in higher flexural strength, whereas samples printed in the in-plane direction showed higher tensile strength. Regarding the effect of infill patterns, Srinivasan et al. [20] observed that the grid pattern outperformed other infill patterns such as line, triangular, cubic, honeycomb, concentric, rectilinear, rectangular, octet, and Wiggle under the tensile load. In another study by Khan et al. [21], it was revealed that the rectilinear pattern outperformed the honeycomb and collinear infill patterns in terms of tensile properties. Fekete et al. [22] studied two different patterns, i.e., line and grid under tensile and impact loads. The former pattern showed higher tensile and impact strength.

The above analysis indicates that only limited studies on the raster angles and their combinations, such as 0/90° and 45/−45°, have been conducted by researchers under flexural loads. Whereas the work related to the effect of infill patterns has only been performed under tensile loads; the other loading conditions have not yet been explored. Therefore, there is a need to study the behavior of different raster angles and infill patterns under flexural loading conditions. The reason behind the evaluation of the in-plane and edgewise (transverse) bending moduli was that there are many applications where the beams are subjected to both types of bending loads. As discussed above, the most common of these applications are in aerospace, especially in aircraft wing spars which are the main loading carrying component of an aircraft wing [23]. They are subjected to in-plane and edgewise flexural loading during the flight of an aircraft, as illustrated in Figure 2. The flexural loads are higher than the other loads on a spar during flight [24]; therefore, it was necessary to determine the raster angle and infill pattern which gave the highest flexural properties. Hence, a range of samples constituting singular as well as a combination of raster angles, i.e., 0°, 90°, 60°, 0/90°, 45/−45°, 60/30°, and 75/15°, were studied experimentally along with five different infill patterns. The raster angles representation with the help of flatwise samples is presented in Figure 3. The results have been quantified in terms of maximum flexural load, flexural modulus, flexural strength, and fracture strain under flexural load.
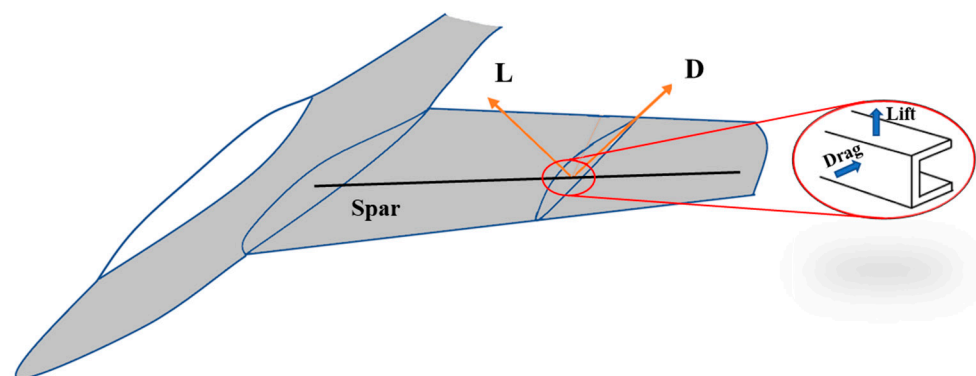

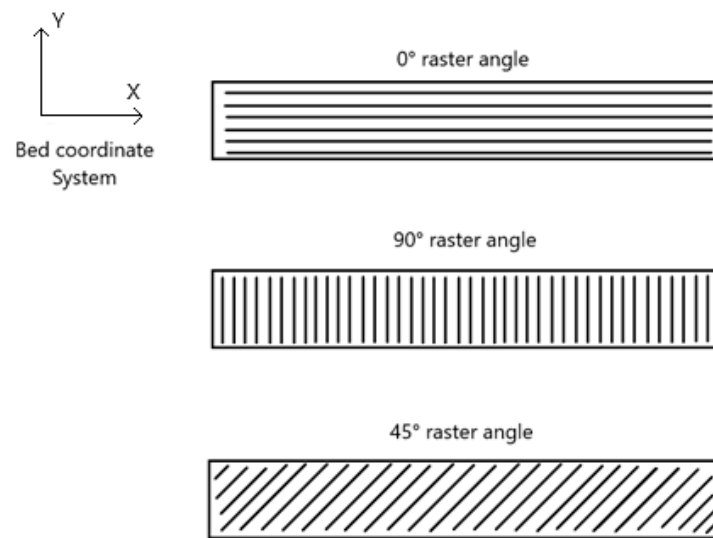**Figure 2.** Wing spar under in-plane and edgewise flexural loading.

Figure 3. Raster angle representation with the help of flatwise samples.

2. Materials and Methods

2.1. Printing of Specimens

Flexural specimens were prepared from SUNLU acrylonitrile–butadiene–styrene (ABS) with a diameter of 1.75 mm. This grade of material corresponds to simple "ABS" as provided by the manufacturer. CreatBot F430 FDM printer was used for the fabrication of these specimens. Dimensions of the specimens were kept as per the guidelines mentioned in ASTM D790 [25]. Samples were designed in PTC Creo CAD software with specified dimensions, as shown in Figure 4, while Ultimaker CURA was used to set process parameters. These process parameters were divided into two categories, i.e., constant and variable. For the effect of raster angle, other printing parameters, including nozzle diameter, layer height, printing speed, nozzle, bed, and chamber temperatures, were kept constant. Samples were printed at raster angles of $0°$, $90°$, $0/90°$, $45/-45°$, $60/30°$, $75/15°$, and $60°$ with an infill density of 100%. Whereas for observing the effect of infill patterns, the infill density was reduced from 100% to 60% so that the effect of infill patterns becomes more pronounced. Samples were printed at five different infill patterns, i.e., line, triangular, grid, tri-hexagon, and quarter-cubic, with an infill density of 60%, as presented in Figure 5. Table 1 summarizes the values of the process parameters used. At the same time, the overall experimental plan is shown in Figure 6.
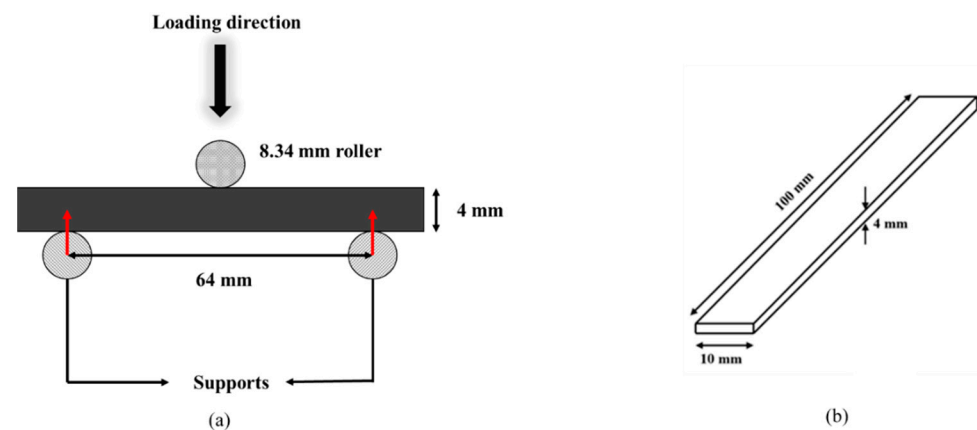

Figure 4. (**a**) Schematic of Experimental Setup; (**b**) dimensions of bending specimen used in this study.
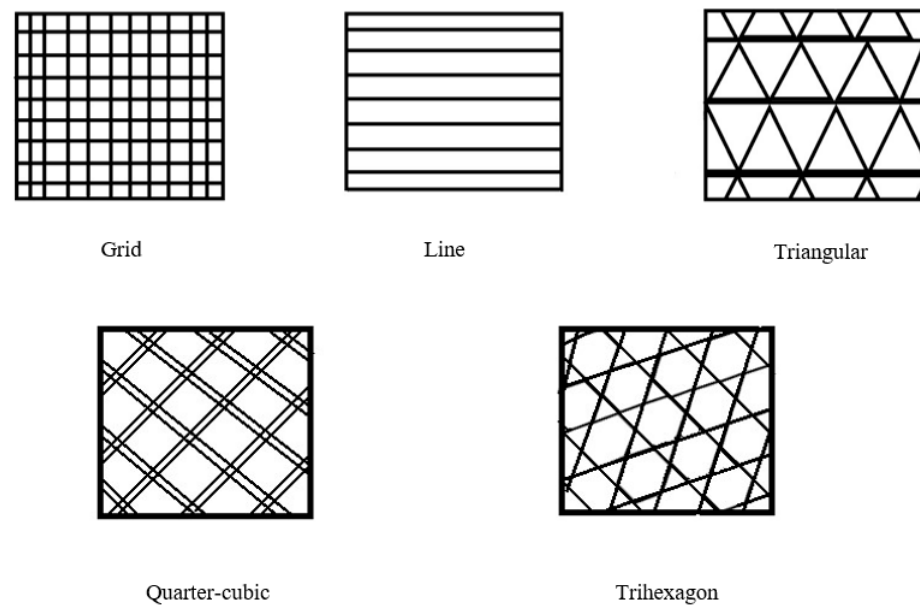
Figure 5. Infill patterns assessed in this study.

Table 1. Process parameters used for 3D printing of specimens in this study.

Process Parameters	Value
Nozzle diameter (mm)	0.4
Layer height (mm)	0.3
Chamber Temperature (°C)	28
Nozzle temperature (°C)	250
Bed temperature (°C)	100
Printing speed (mm/s)	60
Number of bottom layers with 100% infill density (for infill pattern evaluation)	3
Number of top layers 100% infill density (for infill pattern evaluation)	3
Number of layers inner layers contributing to 60% infill density (for infill pattern evaluation) *	8

* It must be noted that, for the samples fabricated for evaluating the effect of infill pattern on the flexural properties, the number of top and bottom layers was 6, i.e., 3 at the bottom and 3 at the top. These layers had 100% infill, while the inner layers were printed with lower infill density, i.e., 60%.
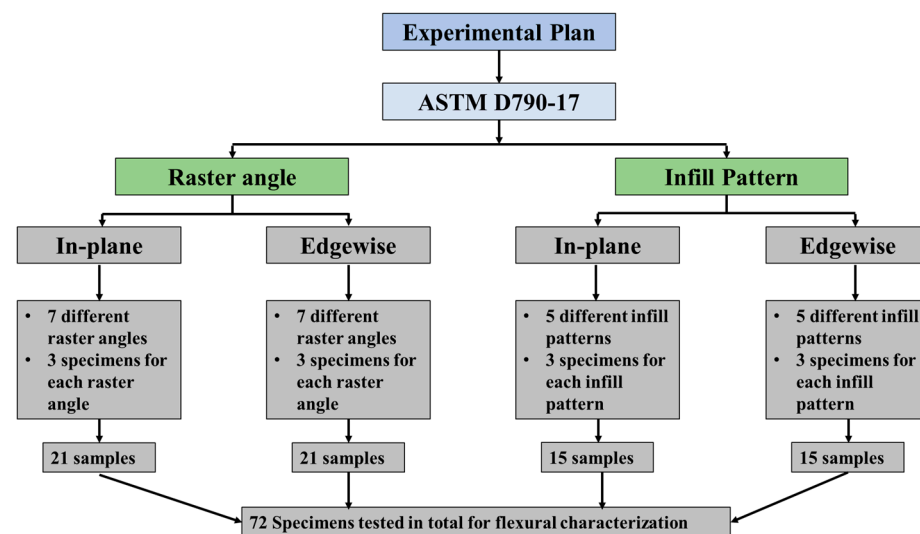

Figure 6. Experimental plan.

2.2. Flexural Test

The 3-point bending test of the specimens was performed using INSTRON 5567. The tests were performed according to ASTM D-790 guidelines at room temperature under a crosshead speed of 2 mm/min. Specimens were tested for in-plane and edgewise bending moduli to assess the effect of raster angle and infill pattern. The experimental setup is shown in Figure 7. The flexural stress–strain behavior was obtained using ASTM D790-10 guidelines using Equations (1) and (2):

$$flexural\ stress = \sigma_f = \frac{3PL}{2bd^2} \tag{1}$$

where P is the load, L is the length between the supports, b is the width of the specimen, d is the depth of the specimen and σ_f is the flexural stress;

$$flexural\ strain = \epsilon_f = \frac{6Dd}{L^2} \tag{2}$$

where D is the maximum deflection at the center of the beam, d is the depth of the beam, L is the length between the supports and ϵ_f flexural strain.
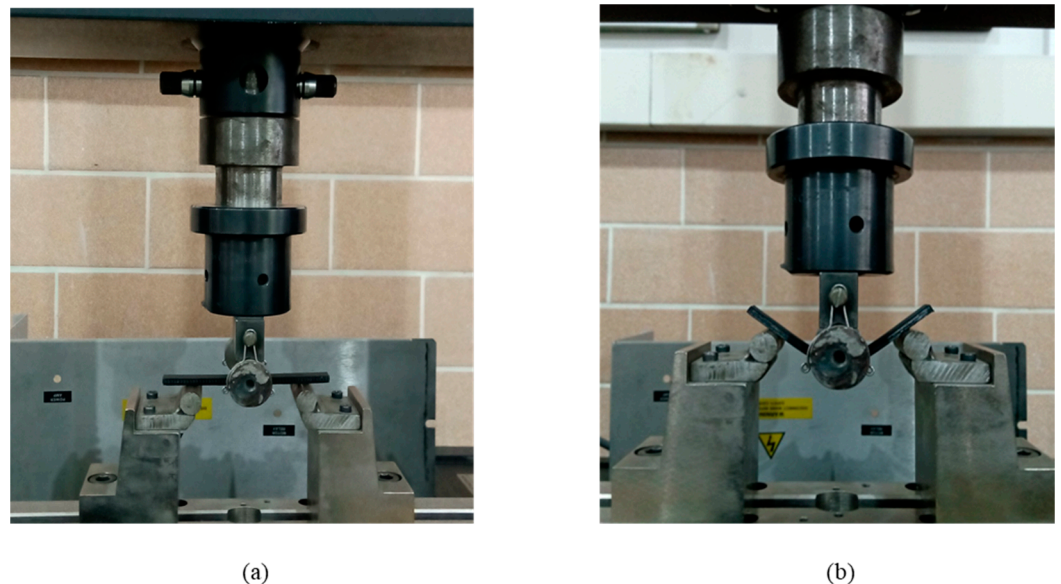

|(a)|(b)|

Figure 7. (**a**) Experimental Setup before the application of load; (**b**) after the application of load.

2.3. Fractographic Analysis

Fractography analysis for the fracture surfaces of different 3D printed samples was carried out on ZEISS EVO 15 Scanning Electron Microscopy (SEM) to analyze the important features. An accelerating voltage of 5kV was used for the imaging process. The samples were non-conductive; therefore, they were sputter-coated using Copper (Cu).

3. Results and Discussion

This study investigated the impact of raster angle and infill pattern on the flexural properties of 3D printed ABS. More than 100 samples were printed. However, samples for the testing need to be free from defects such as warpage and distortion of printed layers; therefore, 72 samples were tested that were deemed suitable for testing conditions. All the results presented in this section are the average of the three specimens tested for each sample type. The effect on the properties was quantified in terms of four main parameters, i.e., maximum flexural load, maximum flexural strength, maximum flexural strain, and flexural modulus. The force displacement data from the experimentation was used to obtain the flexural stress and strain using the formulation given by ASTM D790, i.e., Equations (1)

and (2). Similarly, the guidelines in the same standard were used to determine the flexural modulus for the samples.

3.1. Effect of Raster Angle on Flexural Properties

This section presents the results for the effect of raster angle variation on the flexural properties of the fabricated specimens.

3.1.1. In-Plane Testing

Figure 8 and Table 2 summarize the results for the effect of raster angle on the in-plane flexural properties of the specimens. It can be observed from Figure 8 that samples printed at 0° raster angle outperformed all other raster angles for in-plane testing. The average maximum flexural load and flexural modulus obtained for the 0° raster angle samples came out to be 138.42 ± 3.19 and 3.2 ± 0.01 GPa, respectively. In comparison, the lowest values for these flexural properties were found for samples printed at 90° raster angle. Furthermore, it can be noticed from Table 2 that there was an increase of 188.2% and 148% in the values of maximum flexural load and the flexural modulus, respectively, when the raster angle was shifted from 90° to 0°.
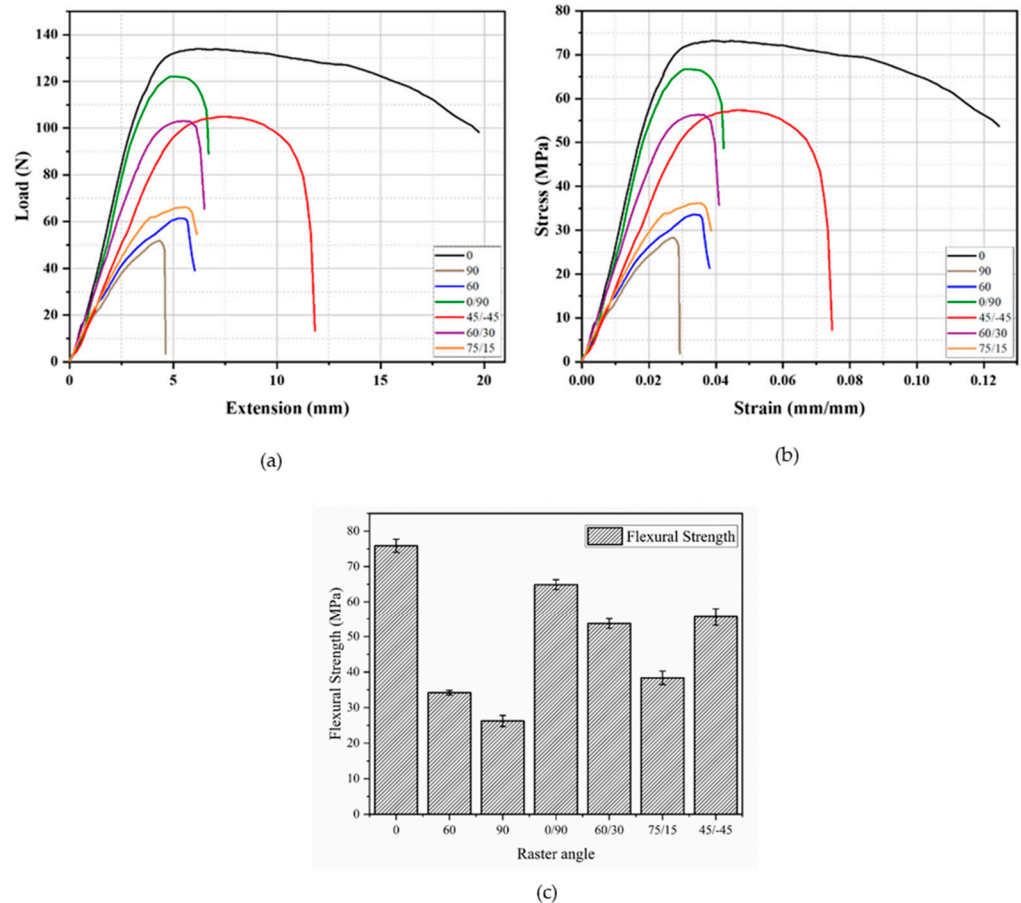

(a)

(b)

(c)

Figure 8. (**a**) In-plane load extension (**b**) in-plane stress–strain behavior for different raster angles; (**c**) comparison of in-plane flexural strength for different raster angles.

Table 2. Experimental results for flexural properties at different raster angles.

Raster Angle (°)	Max. Flexural Load (N)	Flexural Modulus (Gpa)	Flexural Strength (Mpa)	Fracture Strain (%)
0	138.42 ± 3.19	3.2 ± 0.01	75.87 ± 1.88	Fracture did not occur
60	62.52 ± 1.26	1.56 ± 0.02	34.19 ± 0.67	3.59 ± 0.03
90	48.02 ± 2.87	1.29 ± 0.08	26.24 ± 1.57	2.97 ± 0.29
0/90	119.10 ± 2.60	2.80 ± 0.14	64.90 ± 1.40	3.49 ± 0.34
45/−45	101.56 ± 2.61	1.87 ± 0.41	55.64 ± 1.38	5.68 ± 0.13
60/30	98.22 ± 3.45	2.14 ± 0.12	53.69 ± 1.91	3.82 ± 0.12
75/15	70.34 ± 4.66	1.70 ± 0.02	38.37 ± 2.41	3.76 ± 0.12

Figure 8 shows a change of fracture behavior from ductile to brittle as the raster angle changed from 0° to 90°. Figure 8 also indicates that the fracture did not occur for 0° raster angle even at the very high value of strains, whereas 90° samples failed abruptly on the onset of plastic deformation, thus indicating very low values of fracture strains. A decreasing trend for the fracture strains was observed from 0° to 90° raster angle. As the 3D printed specimens act as laminated structures rather than homogeneous and uniform structures, the maximum value of force that can be endured depends upon the raster angle or simply the infill direction and the loading direction. Therefore, in the case of 0° samples, all the layers were perpendicular to the loading and provided greater resistance to deformation. Here, each raster bears the load and acts as a single beam carrying the load. The strength of the 0° specimen (Figure 8c) was the highest for the same reason; however, as the angle approached 90°, the loading axis became parallel to the layers, hence the failure occurred at a lower value of loads. This could be attributed to the ease of shear deformation because, at 90° raster angle, the loading bearing surface is the interface between the rasters, hence the specimens failed along the direction of load.

3.1.2. Edgewise Testing

Edgewise testing was carried out with three raster angles, i.e., 0°, 90° and 0/90°. Results for the maximum edgewise flexural load and strength have been given in Figure 9 and Table 3.

Figure 9 shows the same trend as in the case of in-plane testing. The highest values obtained were for the 0° raster angle, i.e., 73.23 ± 1.36 N and 1.61 ± 0.01 GPa for the flexural load and modulus, respectively, while the lowest values were achieved for the 90° raster angle, i.e., 67.14 ± 2.37 N and 1.51 ± 0.02 GPa. A similar change in the material behavior was observed in this case as well. As indicated by Figure 9b, the behavior changed from ductile to brittle as the raster angle changed from 0° to 90°. The steep decline in the stress–strain curve caused due to the abrupt failure of the samples for the 90° samples shows this transition. An increase of 24.2% in the value of maximum flexural load was observed for the transition of the raster angle from 90° to 0°. Again, this can be attributed to the interaction between the material orientation and the loading direction. The rasters in the case of 0° raster angle were perpendicular to the loading direction, hence the resistance to deformation was high. This also resulted in no fracture for the case of 0° as presented and tabulated in Figure 9b and Table 3, respectively.
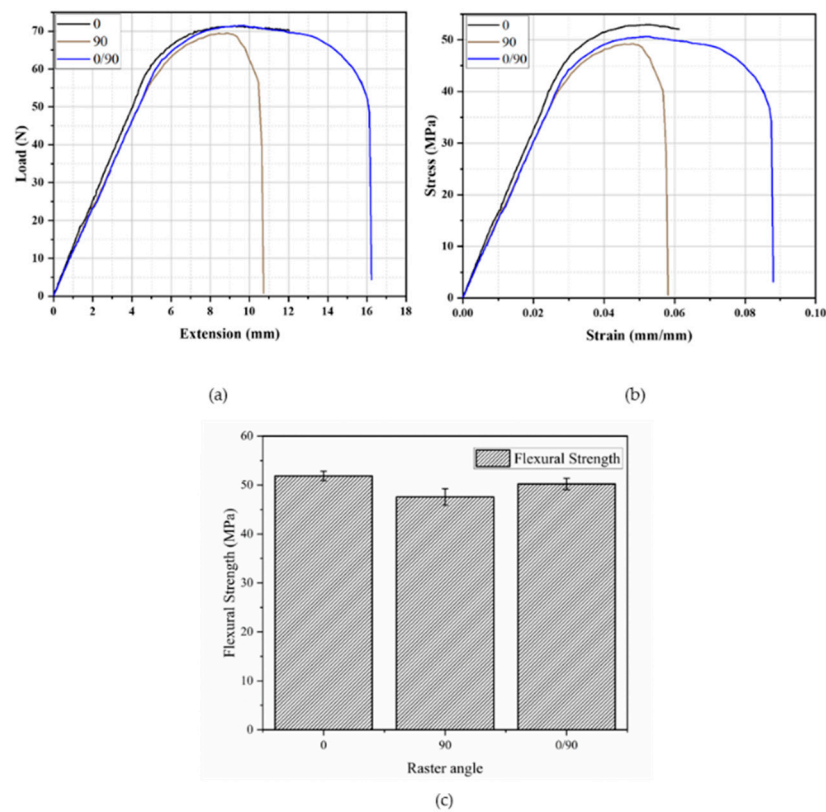
Figure 9. (**a**) Edgewise load extension and (**b**) edgewise stress–strain behavior for different raster angles; (**c**) comparison of edgewise flexural strength for different raster angles.

Table 3. Experimental results for edgewise flexural properties.

Raster Angle (°)	Max. Flexural Load (N)	Flexural Modulus (GPa)	Flexural Strength (MPa)	Fracture Strain (%)
0	73.2 ± 1.36	1.61 ± 0.01	51.9 ± 0.97	Fracture did not occur
90	67.1 ± 2.37	1.51 ± 0.02	47.6 ± 1.68	5.8 ± 0.18
0/90	70.9 ± 1.64	1.53 ± 0.04	50.2 ± 1.16	7.6 ± 0.35

3.2. Effect of Infill Pattern on Flexural Properties

This section presents the results for the effect of infill pattern variation on the flexural properties of the fabricated specimens.

3.2.1. In-Plane Testing

Results for five infill patterns, i.e., line, grid, quarter-cubic, triangular, and tri-hexagon, have been given in Figure 10 and Table 4. The results indicate that, in terms of maximum flexural load, all the infill patterns showed comparable values but the tri-hexagon pattern showed the highest among the tested i.e., 69.0 ± 2.77 N; whereas, when the value for the flexural modulus is compared, it can again be observed that although the values are comparable, the triangular pattern has the highest value for the flexural modulus. A comparison based on the percentage difference between these two patterns indicates that a difference of 7% and 2% existed between these two patterns for flexural modulus and load, respectively. Moreover, the tri-hexagon pattern also showed superior strength under flexural loading, i.e., 36.7 ± 1.22 MPa. Similarly, a difference of only 8.6% and 13% exists between the tri-hexagon and quarter-cubic pattern in terms of flexural load and modulus, respectively. However, it is worth noting that the performance of the infill pattern is highly subjected to the nature of the loading conditions, i.e., whether it is tensile, compressive, or

bending. The pattern performing well for one loading condition may not give an adequate performance for another type of loading. Therefore, it can be safely said that the different infill patterns performed differently under distinct loading conditions.
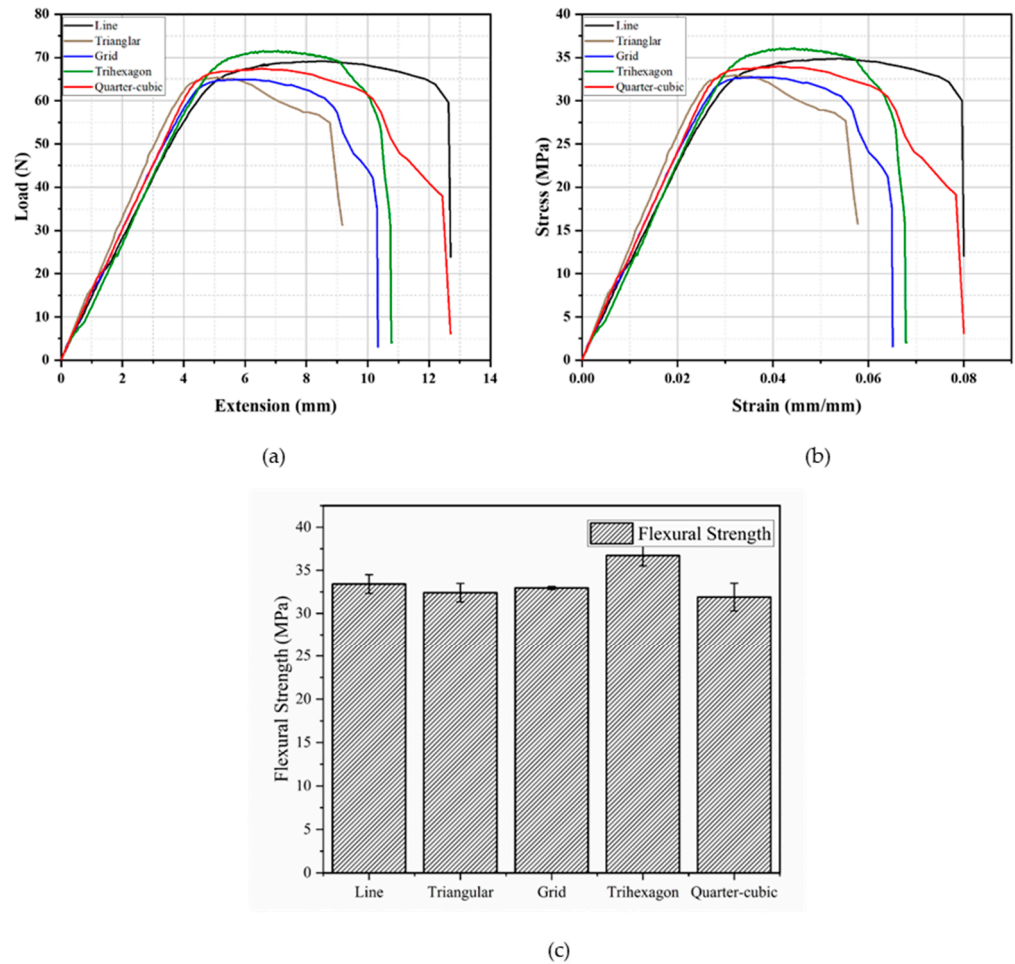

(a)

(b)

(c)

Figure 10. (**a**) In-plane force-extension; (**b**) stress–strain behavior of different infill patterns; (**c**) comparison of in-plane flexural strengths for different infill patterns.

Table 4. Experimental results for in-plane flexural properties at different infill patterns.

Pattern	Max. Flexural Load (N)	Flexural Modulus (GPa)	Flexural Strength (MPa)	Fracture Strain (%)
Line	62.7 ± 2.14	1.06 ± 0.01	33.4 ± 1.08	7.36 ± 0.60
Triangular	64.3 ± 2.12	1.26 ± 0.04	32.4 ± 1.07	4.95 ± 0.40
Grid	65.3 ± 0.32	1.21 ± 0.02	33.0 ± 0.16	5.95 ± 0.69
Tri-hexagon	69.0 ± 2.77	1.23 ± 0.03	36.7 ± 1.22	5.99 ± 0.35
Quarter-cubic	63.3 ± 3.19	1.17 ± 0.03	31.9 ± 1.60	6.03 ± 0.51

3.2.2. Edgewise Testing

The edgewise testing of infill patterns yielded different results compared to the in-plane testing, as presented in Figure 11. Table 5 shows that the highest edgewise flexural modulus was obtained for the quarter-cubic pattern, i.e., 0.38 ± 0.01 GPa, while the lowest flexural modulus of 0.26 ± 0.02 GPa was shown by the tri-hexagon pattern. A similar trend was noticed for the maximum flexural load. A maximum load of 29.1 ± 1.01 N was carried by a quarter-cubic pattern, whereas the tri-hexagon withstood a maximum flexural load of only 11.1 ± 0.90 N. A percentage difference comparison between the two shows that the quarter-cubic pattern outperforms the tri-hexagon pattern by 89% and 37%

in terms of flexural load and modulus, respectively. The trend was also similar for the remaining two parameters, as given in Table 5. This could be possible due to the high degree of bonding between the layers of the quarter-cubic pattern and the higher stiffness demonstrated by the individual cubic cells formed in the quarter-cubic pattern, which has been discussed in detail with the help of SEM micrographs presented in the next section. Moreover, quarter-cubic exhibited a ductile behavior among the tested patterns, as illustrated in Figure 11b.
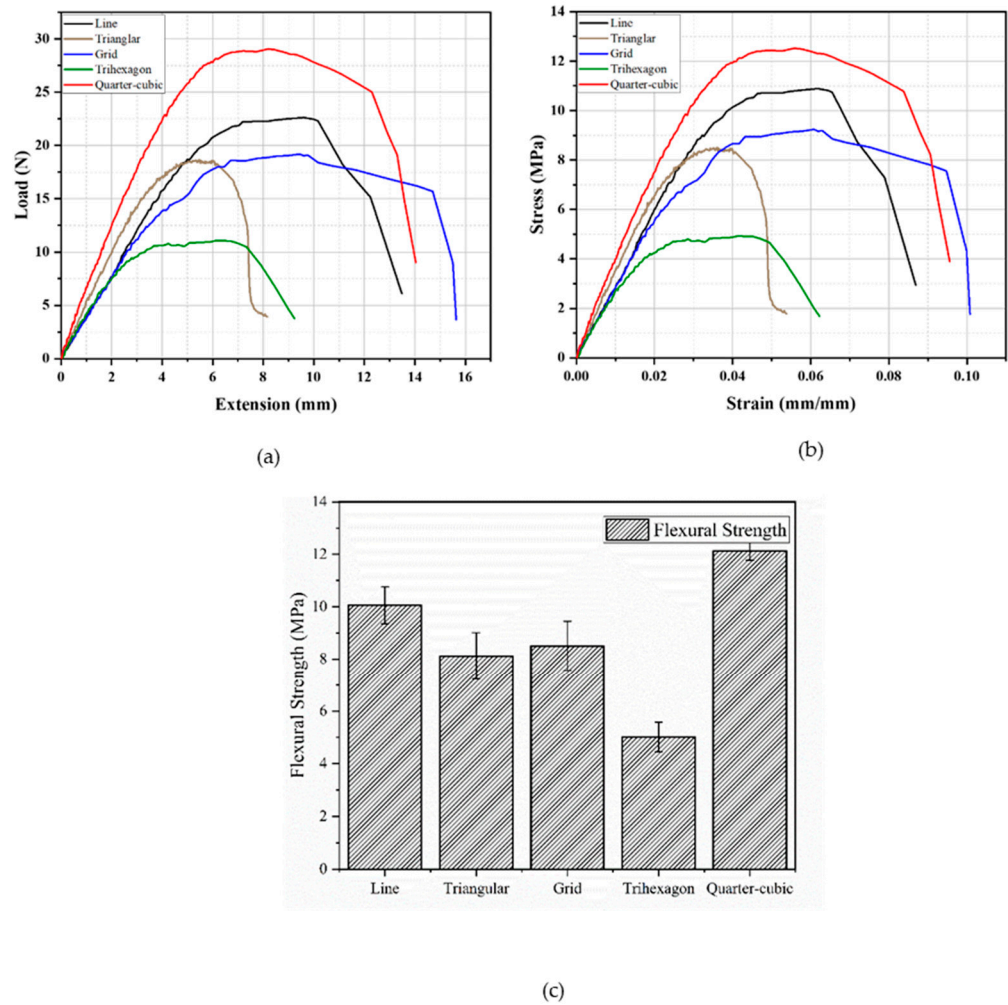

(a)

(b)

(c)

Figure 11. (**a**) Edgewise force-extension; (**b**) stress–strain behavior of different infill patterns; (**c**) Comparison of Edgewise flexural strengths for different infill patterns.

Table 5. Summary of Experimental results for edgewise flexural properties at different infill patterns.

Pattern	Max. Flexural Load (N)	Flexural Modulus (GPa)	Flexural Strength (MPa)	Fracture Strain (%)
Line	22.6 ± 1.25	0.28 ± 0.01	10.1 ± 0.70	6.7 ± 0.1
Triangular	18.9 ± 1.74	0.32 ± 0.02	8.12 ± 0.89	4.8 ± 0.1
Grid	19.2 ± 1.52	0.27 ± 0.01	8.51 ± 0.94	9.4 ± 1.2
Tri-hexagon	11.1 ± 0.90	0.26 ± 0.02	5.01 ± 0.56	5.0 ± 0.1
Quarter-cubic	29.0 ± 1.01	0.38 ± 0.01	12.1 ± 0.36	8.3 ± 0.1

3.2.3. Fractographic Analysis

To further investigate the flexural behavior of the specimens, the fractographic analysis was performed using SEM, as shown in Figure 12. In addition, raster angles for which

the mechanics have not been studied in detail were analyzed. For the analysis of the in-plane sample, the samples with raster angles of $45/-45°$ and $75/15°$ were analysed, whereas quarter-cubic and tri-hexagon specimens were analyzed for the infill pattern case, as depicted in Figure 12e,f. The micrographs revealed the presence of three different types of defect in the tested samples, which are categorized as delamination between consecutive layers (1), raster rupture (2) and voids or gaps (3), as shown in Figure 12. These defects, in turn, affected the fracture behavior of the samples.
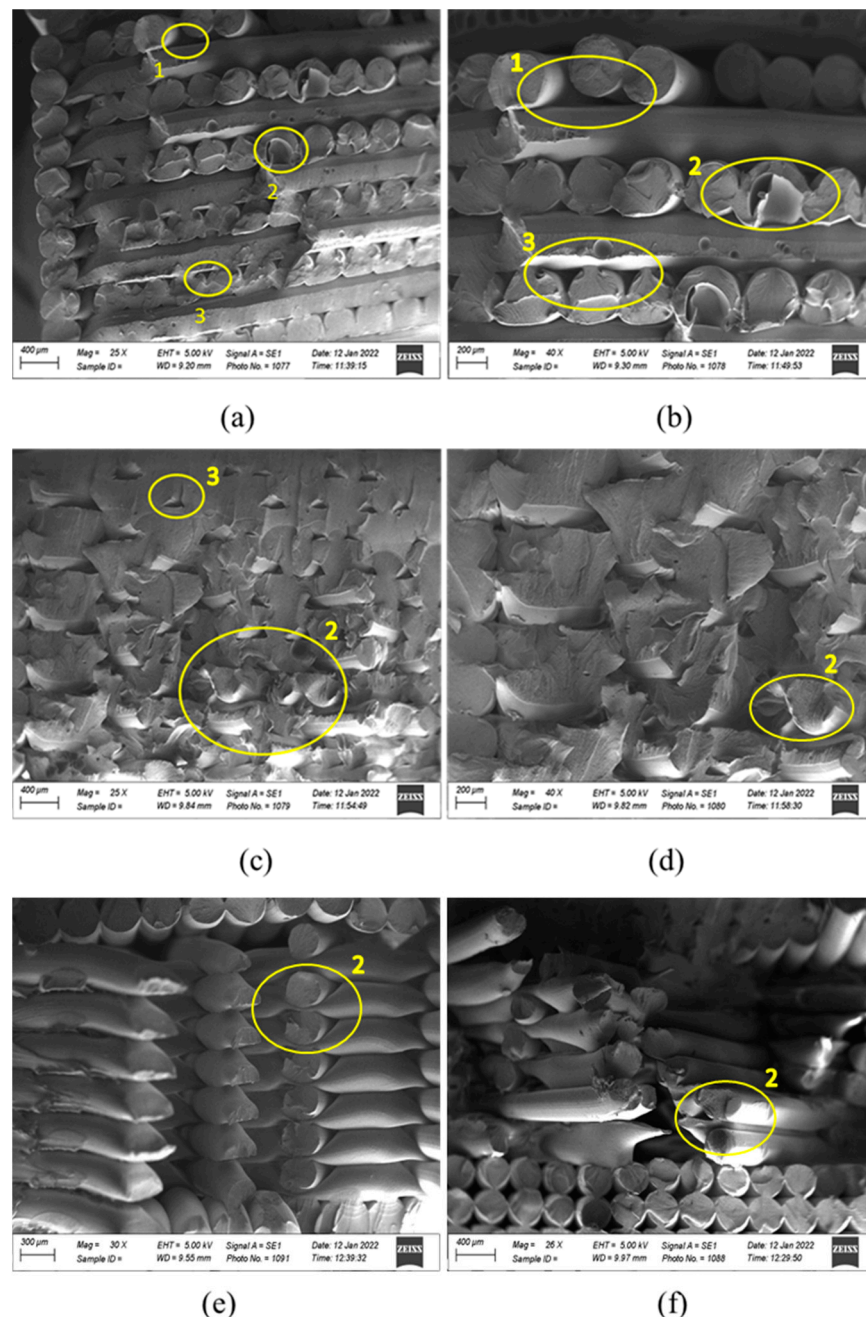

Figure 12. Fractographic analysis of 3D printed Samples (**a**) 75/15 at 25× magnification; (**b**) 75/15 at 40× magnification; (**c**) 45/−45 at 25× magnification; (**d**) 45/−45 at 40× magnification; (**e**) quarter-cubic pattern micrograph; (**f**) Tri-hexagon pattern micrograph.

Delamination is commonly observed due to weak interlayer bonding or when the load applied exceeds the energy required to overcome the interlayer bonding; thus, delamination can lead to the formation of further gaps and voids between the layers, which cause stress

concentrations and hence the failure. The failure of individual rasters due to severe loading conditions was categorized as a raster rupture, whereas the presence of the inherent voids and gaps (3), as shown in Figure 12**a,c**, is due to the nature of the manufacturing process, i.e., fused filament fabrication. Although the infill density was theoretically set to 100%, some voids are still there due to the different process parameters, such as the printing speed and raster gap. These voids act as the stress raisers and stress concentration regions where the fracture can preferentially occur. Similar mechanisms have also been reported in the literature for the 3D printed polymeric materials under different loading conditions. However, in the case of $45/-45°$, good interlayer bonding and no periodic voids can be seen, hence providing greater strength than $75/15°$ [26].

Similarly, for the quarter-cubic and the tri-hexagon, the micrographs show that the raster rupture was more drastic (along with the presence of voids) and hence the major mechanism for failure. Furthermore, the surfaces of the raptured rasters also indicated a brittle fracture in the tri-hexagon pattern, resulting in a significant difference in the flexural load carrying capacity for edgewise samples.

4. Conclusions

Additive manufacturing is being utilized for advancements in the aerospace and automotive fields. In the case of aerospace structures where the loading is flexural as well as bi-directional in nature, it is vital to ensure structural integrity in both directions. The geometrical parameters play an important role in the determination of the stresses; however, the material properties under the particular loading conditions are also of great significance, as the introduction of anisotropy in components produced by fused filament fabrication (FFF) is a common attribute that affects the mechanical properties of the components. Therefore, in this study, the effects of two important parameters which define the material deposition strategy in the FFF process were evaluated under flexural loading conditions. The results were quantified for the in-plane and edgewise directions in terms of maximum flexural load, flexural strength, and flexural modulus of the material. This helped form the basis of a guideline for the researchers working in aerospace structures via additive manufacturing. The following findings can be concluded from this study:

- The samples with 0° raster angle sustained the highest in-plane and edgewise flexural load among all tested raster angles. The increase in the load carrying capacity at 0° was 188% greater than that at 90°;
- 0° raster angle exhibited the highest in-plane/edgewise flexural modulus. In-plane flexural modulus increased by about 148% when the raster angle was changed from 90° to 0°;
- Overall, the edgewise flexural modulus of acrylonitrile–butadiene–styrene (ABS) was lower than the in-plane flexural modulus. However, the trend was similar, i.e., the highest edgewise flexural modulus was also obtained for the 0° raster angle;
- For the infill patterns, the percentage difference comparison was used to evaluate the most optimum infill pattern for the flexural loading conditions. This comparison indicated that, for both the flexural load and modulus in both directions, the quarter-cubic pattern was the optimum choice for components such as structural components subjected to bi-directional flexural loading conditions. This is because the quarter-cubic pattern outperformed the tri-hexagon pattern by 89% and 37% in terms of flexural load and modulus, respectively;
- The difference in the properties in the two directions for every parameter indicates that the additive manufacturing processes, especially the FFF process, cause a significant degree of anisotropy in the fabricated components. Hence, this study was of fundamental importance to serve as a guideline where AM for the design of structural components subjected to flexural loading conditions is utilized.

References

1. Vafadar, A.; Guzzomi, F.; Rassau, A.; Hayward, K. Advances in Metal Additive Manufacturing: A Review of Common Processes, Industrial Applications, and Current Challenges. *Appl. Sci.* **2021**, *11*, 1213. [CrossRef]
2. Gohar, S.; Hussain, G.; Ilyas, M.; Ali, A. Performance of 3D printed topologically optimized novel auxetic structures under compressive loading: Experimental and FE analyses. *J. Mater. Res. Technol.* **2021**, *15*, 394–408. [CrossRef]
3. Ahmed, S.W.; Hussain, G.; Al-Ghamdi, K.A.; Altaf, K. Mechanical properties of an additive manufactured CF-PLA/ABS hybrid composite sheet. *J. Thermoplast. Compos. Mater.* **2019**, *34*, 1577–1596. [CrossRef]
4. Habib, N.; Siddiqi, M.; Muhammad, R. Thermal simulation of grain during selective laser melting process in 3D metal printing. *J. Eng. Appl. Sci.* **2020**, *39*, 14–21. [CrossRef]
5. *ISO/ASTM 52900:2015;* Additive Manufacturing-General Principles-Terminologies. ISO: Geneva, Switzerland, 2015. Available online: https://www.iso.org/standard/69669.html (accessed on 20 March 2022).
6. Gohar, S.; Hussain, G.; Ali, A.; Ahmad, H. Mechanical performance of honeycomb sandwich structures built by FDM printing technique. *J. Thermoplast. Compos. Mater.* **2021**. [CrossRef]
7. Ahmed, H.; Hussain, G.; Gohar, S.; Ali, A.; Alkahtani, M. Impact Toughness of Hybrid Carbon Fiber-PLA/ABS Laminar Composite Produced through Fused Filament Fabrication. *Polymers* **2021**, *13*, 3057. [CrossRef] [PubMed]
8. Kamaal, M.; Anas, M.; Rastogi, H.; Bhardwaj, N.; Rahaman, A. Effect of FDM process parameters on mechanical properties of 3D-printed carbon fibre–PLA composite. *Prog. Addit. Manuf.* **2021**, *6*, 63–69. [CrossRef]
9. Solomon, I.J.; Sevvel, P.; Gunasekaran, J. A review on the various processing parameters in FDM. *Mater. Today Proc.* **2021**, *37*, 509–514. [CrossRef]
10. Venkatraman, R.; Raghuraman, S. Experimental analysis on density, micro-hardness, surface roughness and processing time of Acrylonitrile Butadiene Styrene (ABS) through Fused Deposition Modeling (FDM) using Box Behnken Design (BBD). *Mater. Today Commun.* **2021**, *27*, 102353.
11. Ramezani Dana, H.; El Mansori, M.; Barrat, M.; Seck, C. Tensile behavior of additively manufactured carbon fiber reinforced polyamide-6 composites. *Polym.-Plast. Technol. Mater.* **2022**, *61*, 624–641.
12. Balderrama-Armendariz, C.O.; MacDonald, E.; Espalin, D.; Cortes-Saenz, D.; Wicker, R.; Maldonado-Macias, A. Torsion analysis of the anisotropic behavior of FDM technology. *Int. J. Adv. Manuf. Technol.* **2018**, *96*, 307–317. [CrossRef]
13. Azammi, A.N.; Ilyas, R.; Sapuan, S.; Ibrahim, R.; Atikah, M.; Asrofi, M.; Atiqah, A. Characterization studies of biopolymeric matrix and cellulose fibres based composites related to functionalized fibre-matrix interface. In *Interfaces in Particle and Fibre Reinforced Composites*; Woodhead Publishing: Sawston, UK, 2020; pp. 29–93.
14. Byberg, K.I.; Gebisa, A.W.; Lemu, H.G. Mechanical properties of ULTEM 9085 material processed by fused deposition modeling. *Polym. Test.* **2018**, *72*, 335–347. [CrossRef]
15. Kaplun, B.W.; Zhou, R.; Jones, K.W.; Dunn, M.L.; Yakacki, C.M. Influence of orientation on mechanical properties for high-performance fused filament fabricated ultem 9085 and electro-statically dissipative polyetherketoneketone. *Addit. Manuf.* **2020**, *36*, 101527. [CrossRef]
16. Motaparti, K.P.; Taylor, G.; Leu, M.C.; Chandrashekhara, K.; Castle, J.; Matlack, M. Experimental investigation of effects of build parameters on flexural properties in fused deposition modelling parts. *Virtual Phys. Prototyp.* **2017**, *12*, 207–220. [CrossRef]
17. Taylor, G.; Wang, X.; Mason, L.; Leu, M.C.; Chandrashekhara, K.; Schniepp, T.; Jones, R. Flexural behavior of additively manufactured Ultem 1010: Experiment and simulation. *Rapid Prototyp. J.* **2018**, *24*, 1003–1011. [CrossRef]
18. Wu, W.; Geng, P.; Li, G.; Zhao, D.; Zhang, H.; Zhao, J. Influence of layer thickness and raster angle on the mechanical properties of 3D-printed PEEK and a comparative mechanical study between PEEK and ABS. *Materials* **2015**, *8*, 5834–5846. [CrossRef]
19. Durgun, I.; Ertan, R. Experimental investigation of FDM process for improvement of mechanical properties and production cost. *Rapid Prototyp. J.* **2014**, *20*, 228–235. [CrossRef]
20. Srinivasan, R.; Kumar, K.N.; Ibrahim, A.J.; Anandu, K.; Gurudhevan, R. Impact of fused deposition process parameter (infill pattern) on the strength of PETG part. *Mater. Today Proc.* **2020**, *27*, 1801–1805. [CrossRef]

21. Khan, S.A.; Siddiqui, B.A.; Fahad, M.; Khan, M.A. Evaluation of the effect of infill pattern on mechanical strength of additively manufactured specimen. In *Materials Science Forum*; Trans Tech Publications Ltd.: Zurich, Switzerland, 2017; pp. 128–132.

22. Fekete, I.; Ronkay, F.; Lendvai, L. Highly toughened blends of poly (lactic acid)(PLA) and natural rubber (NR) for FDM-based 3D printing applications: The effect of composition and infill pattern. *Polym. Test.* **2021**, *99*, 107205. [CrossRef]

23. Grbović, A.; Kastratović, G.; Sedmak, A.; Balać, I.; Popović, M.D. Fatigue crack paths in light aircraft wing spars. *Int. J. Fatigue* **2019**, *123*, 96–104. [CrossRef]

24. Fujii, K.; Yokozeki, T.; Arizono, H.; Tamayama, M. Fundamental Study on Adaptive Wing Structure for Control of Wing Load Distribution. *Trans. Jpn. Soc. Aeronaut. Space Sci. Aerosp. Technol. Jpn.* **2017**, *15*, a83–a88. [CrossRef]

25. *ASTM D790-02*; Standard Test Methods for Flexural Properties of Unreinforced and Reinforced Plastics and Electrical Insulating Materials. ASTM International: West Conshohocken, PA, USA, 2002.

26. Akhoundi, B.; Behravesh, A.H. Effect of filling pattern on the tensile and flexural mechanical properties of FDM 3D printed products. *Exp. Mech.* **2019**, *59*, 883–897. [CrossRef]